Deep search for glycine conformers in Barnard 5

Citation for the original published paper (version of record):
Carl, T., Wirström, E., Bergman, P. et al (2023). Deep search for glycine conformers in Barnard 5. Monthly Notices of the Royal Astronomical Society, 524(4): 5993-6003.
http://dx.doi.org/10.1093/mnras/stad2017

Monthly Notices of the ROYAL ASTRONOMICAL SOCIETY

MNRAS **524,** 5993–6003 (2023) https://doi.org/10.1093/mnras/stad2017
Advance Access publication 2023 July 17

Deep search for glycine conformers in Barnard 5

Tadeus Carl,[1]★ E. S. Wirström,[1] P. Bergman,[1] S. B. Charnley,[2] Y.-L. Chuang[3] and Y.-J. Kuan[3]

[1]*Onsala Space Observatory, Department of Space, Earth and Environment, Chalmers University of Technology, SE-439 92, Onsala, Sweden*
[2]*Astrochemistry Laboratory and the Goddard Center for Astrobiology, Mailstop 691, 8800 Greenbelt Road, Greenbelt, MD 20770, USA*
[3] *Department of Earth Sciences, National Taiwan Normal Univesity, No. 88, Ting-Chou Rd, Wen-Shan District, Taipei City, Taiwan 11677, China*

Accepted 2023 June 30. Received 2023 June 30; in original form 2023 May 25

ABSTRACT

One of the most fundamental hypotheses in astrochemistry and astrobiology states that crucial biotic molecules like glycine (NH_2CH_2COOH) found in meteorites and comets are inherited from early phases of star formation. Most observational searches for glycine in the interstellar medium have focused on warm high-mass molecular cloud sources. However, recent studies suggest that it might be appropriate to shift the observational focus to cold low-mass sources. We aim to detect glycine towards the so-called methanol hotspot in the Barnard 5 dark cloud. The hotspot is a cold source ($T_{\rm gas} \approx 7.5$ K) with yet high abundances of complex organic molecules (COMs) and water in the gas phase. We carried out deep pointed observations with the Onsala 20 m telescope, targeting several transitions of glycine conformers I and II (Gly-I and Gly-II) in the frequency range 70.2–77.9 GHz. No glycine lines are detected towards the targeted position, but we use a line stacking procedure to derive sensitive abundance upper limits w.r.t. H_2 for Gly-I and Gly-II, i.e. $\leq(2\text{–}5) \times 10^{-10}$ and $\leq(0.7\text{–}3) \times 10^{-11}$, respectively. The obtained Gly-II upper limits are the most stringent for a cold source, while the Gly-I upper limits are mostly on the same order as previously measured limits. The measured abundances w.r.t. H_2 of other COMs at the B5 methanol hotspot range from 2×10^{-10} (acetaldehyde) to 2×10^{-8} (methanol). Hence, based on a total glycine upper limit of $(2\text{–}5) \times 10^{-10}$, we cannot rule out that glycine is present but undetected.

Key words: astrobiology – astrochemistry – ISM: abundances – ISM: molecules.

1 INTRODUCTION

Glycine (NH_2CH_2COOH) is the simplest amino acid used in the metabolism of terrestrial lifeforms. Since its first detection in meteorites in the 1970s (Kvenvolden et al. 1970; Cronin & Pizzarello 1999; Ehrenfreund et al. 2001; Botta et al. 2002; Glavin et al. 2006; Koga & Naraoka 2017) it has been speculated that prebiotic materials have been delivered to Earth by smaller impacting bodies (Hoyle & Wickramasinghe 1977; Ehrenfreund & Charnley 2000). This hypothesis is supported by the identification of glycine in the comas of comets 81P/Wild 2 (Elsila, Glavin & Dworkin 2009) and 67P/Churyumov–Gerasimenko (Altwegg et al. 2016; Hadraoui et al. 2019), as well as in samples from asteroid (162173) Ryugu (Naraoka et al. 2023). There is general consensus that meteoric glycine is mainly the product of aqueous alteration in subsurface layers of the asteroidal host bodies (Lee et al. 2009; Ioppolo et al. 2021, and references therein). On the other hand, the study by Hadraoui et al. (2019) suggests that cometary glycine is more pristine and might indeed have an interstellar origin.

To test the claimed hypothesis, astronomers have searched for signs of interstellar amino acids, in particular glycine, for more than four decades (Brown et al. 1979; Hollis et al. 1980; Snyder et al. 1983; Berulis et al. 1985; Guélin & Cernicharo 1989; Combes, Rieu & Wlodarczak 1996; Ceccarelli et al. 2000; Hollis et al. 2003a, b; Kuan et al. 2003; Snyder et al. 2005; Cunningham et al. 2007; Jones et al. 2007; Belloche et al. 2008; Guélin et al. 2008; Drozdovskaya et al. 2019; Jiménez-Serra et al. 2020). However, no clear detection has been made to this day. Most studies have focused on high-mass star-forming regions (especially hot cores in Sgr B2 and Ori A), although some low-mass dark cloud sources have been included in the sample sets of Brown et al. (1979) and Snyder et al. (1983). Only Ceccarelli et al. (2000) and Drozdovskaya et al. (2019) investigated low-mass protostellar sources (hot corinos).

Hot cores with kinetic temperatures of 100–200 K are often the first choice when searching for complex organic molecules (COMs) due to the overall large amount of available material combined with a rich chemistry and line variety. In the case of glycine, the observational focus on hot cores has been justified by early theoretical (Sorrell 2001; Woon 2002; Garrod 2013) and experimental (Bernstein et al. 2002; Muñoz Caro et al. 2002; Holtom et al. 2005; Lee et al. 2009) studies, indicating that glycine could only form by means of energetic (UV/electron/thermal) processing of interstellar ices, involving temperatures >50 K. There is, however, increasing evidence that a shift of focus to cold (∼10 K) low-mass sources might be appropriate when searching for glycine.

It is known from observations since the 1980s that COMs like methanol (CH_3OH), acetaldehyde (CH_3CHO), or methyl formate (CH_3OCHO) can reach significant abundances in cold molecular cloud sources such as TMC-1, L1689B, L1544, and Barnard 5 (Matthews, Friberg & Irvine 1985; Friberg et al. 1988; Marcelino et al. 2007; Bacmann et al. 2012; Vastel et al. 2014; Jiménez-Serra

★ E-mail: tadeus.carl@chalmers.se

et al. 2016; Taquet et al. 2017). Based on that high degree of chemical complexity, Jiménez-Serra et al. (2014) tested the detectability of glycine with radiative transfer models for the prototypical pre-stellar core L1544, indicating that several glycine transitions with an upper level energy $E_u < 30$ K and an Einstein coefficient of spontaneous emission $A_{ul} \geq 10^{-6}$ s^{-1} can reach detectable intensities in cold sources. Furthermore, severe observational issues with hot cores, such as line blending and multiple velocity components, can be avoided when observing colder, quiescent sources with lower line densities and narrower line widths. In addition, a combined experimental and theoretical study by Ioppolo et al. (2021) has recently shown for the first time that glycine can form on the surface of interstellar ices at low temperatures (∼13 K) and in the absence of energetic irradiation. Experiments and modelling agree that the main route of formation is the radical–radical reaction

$$NH_2CH_2 + HOCO \longrightarrow NH_2CH_2COOH. \quad (1)$$

As many molecules, glycine has several stable conformational isomers with different zero-point energies. The two lowest-energy conformers of glycine are denoted with I and II (hereafter, Gly-I and Gly-II). The zero-point energy of Gly-II is approximately 1007 ± 101 K higher than that of the lower energy conformer Gly-I, while the electric dipole moment of Gly-II is approximately six times higher than that of Gly-I (Lovas et al. 1995). Since spectral intensity is proportional to the square of the dipole moment, the intensity of Gly-II is enhanced by a factor of approximately 36 over Gly-I. This leads to an anomalous high intensity ratio of both conformers, i.e. a much weaker rotational spectrum of Gly-I compared to Gly-II, despite the lower zero-point energy of Gly-I (cf. Snyder et al. 1983). For this reason, Gly-II was the first conformer to be spectroscopically identified in the laboratory (Brown et al. 1978; Suenram & Lovas 1978; Suenram & Lovas 1980). It is also for this reason that early searches for glycine in the interstellar medium (ISM; Brown et al. 1979; Snyder et al. 1983; Berulis et al. 1985) focused on transitions of Gly-II, while all later studies focused either on Gly-I or included transitions of both conformers.

Based on the spectroscopic properties of Gly-I and Gly-II, and on purely thermodynamic grounds, much higher abundances of Gly-I are expected over the whole molecular cloud temperature range (10–200 K). However, observations have shown that an equilibrium isomerization is not always established in molecular clouds, but rather that the high-energy conformer of a molecule can have much higher abundances than expected (García de la Concepción et al. 2022). In the case of formic acid (HCOOH), the gas phase abundance ratio of the high-energy *c*(*is*)-conformer to the low-energy *t*(*rans*)-conformer can reach values of 5–6 per cent, as found towards two dark cloud sources, Barnard 5 and L483, with kinetic temperatures of around 10 K (Taquet et al. 2017; Agúndez et al. 2019). Those ratios are several tens of orders of magnitude higher than predicted by gas phase isomerization models including ground-state quantum tunnelling effects (García de la Concepción et al. 2022). This indicates that some key isomerization mechanisms are not fully understood. Photoswitching mechanisms as proposed by Cuadrado et al. (2016) can likely be neglected in well-shielded dark cloud regions as B5 and L483. However, Taquet et al. (2017) suggest that the solid-state formation of molecules on interstellar ices can produce non-equilibrium isomerizations because the outcome of a surface reaction depends also on the relative orientation between a surface species and the incoming gas phase species (e.g. Rimola, Sodupe & Ugliengo 2012; Enrique-Romero et al. 2016). Furthermore, in the particular case of formic acid, it is assumed that one major route of solid-state formation is the reaction chain

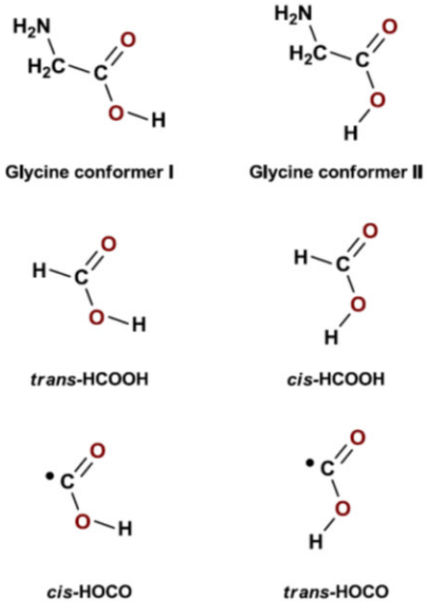

Figure 1. Schematic view of the conformers of parent and daughter molecules in the considered reactions that form glycine (NH_2CH_2COOH) and formic acid (HCOOH) on an interstellar ice surface. Left column: hydrogenation of *c*-HOCO leads to *t*-HCOOH, while the radical–radical reaction NH_2CH_2 + *c*-HOCO leads to Gly-I. Right column: hydrogenation of *t*-HOCO leads to *c*-HCOOH, and NH_2CH_2 + *t*-HOCO forms Gly-II. Credit: Jose Aponte.

$$CO + OH \longrightarrow HOCO, \quad (2)$$

$$HOCO + H \longrightarrow HCOOH, \quad (3)$$

with most of the HOCO radical formed in its low-energy *trans*-configuration (Goumans, Uppal & Brown 2008). However, the hydrogenation of *t*-HOCO leads to *c*-HCOOH, which can significantly increase the gas phase *cis*/*trans* ratio of formic acid, once desorbed from the grain surface. We argue that the same principles can lead to anomalously high Gly-II/Gly-I gas phase ratios in cold sources like B5, if it is assumed that glycine forms in the solid phase via reaction (1), and by noting that Gly-II is formed from reactions of *t*-HOCO and NH_2CH_2 (cf. Fig. 1). However, recent modelling work by Garrod et al. (2022) suggests that several other glycine formation routes can be very efficient at dark cloud conditions and potentially dominate over reaction (1). Of these, only the reaction of NH_2 (or of NH followed by H) with CH_2COOH could lead to glycine conformers I and II since the latter radical is itself formed from HOCO. Thus, in this case, the Gly-II/Gly-I ratio should also follow the *c*/*t*-HCOOH. Therefore, gas phase observations of the Gly-II/Gly-I ratio in cold sources could in principle be used to investigate the main formation routes of glycine at low temperatures.

Based on the above considerations, the methanol hotspot[1] in the Barnard 5 (hereafter B5) dark cloud (Perseus, $d = 302 \pm 21$ pc; Zucker et al. 2018) is a promising target to search for interstellar glycine. It is located approximately 0.55 pc to the northwest of the prominent class-I protostar IRS-1 (see maps in Wirström et al. 2014; Taquet et al. 2017). The location of the hotspot is neither

[1]Following Wirström et al. (2014), the term methanol 'hotspot' is used to indicate the position of the methanol intensity peak.

associated with a prestellar core nor a protostellar source (Wirström et al. 2014, and references therein). The detection of abundant water (8×10^{-9}) by Wirström et al. (2014) as well as methanol (2×10^{-8}) and other COMs ($\sim 10^{-10}$) by Taquet et al. (2017) confirms the chemical complexity of the region; abundances are relative to H_2. In addition, it is in this position that *c*-HCOOH has been detected at a relative abundance of 6 per cent as compared to *t*-HCOOH (Taquet et al. 2017). The H_2 column density and dust temperature towards the hotspot are estimated from data of the Herschel Gould Belt survey[2] (HGBS) as $N(H_2) = 1 \times 10^{22}\,\mathrm{cm^{-2}}$ and $T_{\rm dust} = 13\,\mathrm{K}$, respectively[3] (André et al. 2010; Roy et al. 2014). Non-local thermodynamic equilibrium (LTE) radiative transfer calculations of methanol emission by Taquet et al. (2017) reveal a gas kinetic temperature of $T_{\rm kin} = 7.5 \pm 1.5\,\mathrm{K}$ and a gas density of $n(H_2) = (2.25 \pm 1.50) \times 10^5\,\mathrm{cm^{-3}}$.

For our study, single-point observations were made with the Onsala 20 m telescope towards the B5 hotspot, with several Gly-I and Gly-II transitions targeted in the frequency range ~70–78 GHz. The observations are described in Section 2, and we present the resulting spectrum and the detected molecules in Section 3. Glycine was not detected, but we derive sensitive upper limits for both glycine conformers using spectral line stacking, as described in Section 4. In that section, we also present the column density calculation for other detected molecules. In Section 5, the derived glycine upper limits are compared to limits for other sources as well as to reported abundances of other COMs at the position of the B5 hotspot. We summarize our conclusions in Section 6.

2 OBSERVATIONS

Our LTE analysis using $T_{\rm ex} = 7.5\,\mathrm{K}$ predicts that a number of Gly-I and Gly-II transitions in the 4 mm band will have detectable peak intensities if the glycine abundance and distribution at the B5 hotspot is similar to other detected COMs (Taquet et al. 2017). The considered transitions are presented in Table 1 with their spectroscopic properties. Single point observations were carried out towards the B5 hotspot with the Onsala 20 m telescope at 70.2–77.9 GHz. We observed for a total of ~150 h in three observation runs in 2017, 2018, and 2022.

The receiver frontend was a 4 mm dual-polarization sideband-separating HEMT receiver (Walker et al. 2016). This frontend has common warm optics with the 3 mm system (Belitsky et al. 2015). In the 2017 observations, the centre frequency was 72 GHz, and in 2018, it was 76 GHz. In the 2022 observations, we used two settings with the centre frequencies from 2017 and 2018, referred to as S1 and S2, respectively. We used a symmetric dual-beam switching mode with a switching frequency of 1 Hz and a beam throw of 11 arcmin in azimuth. The half-power beamwidth at 74 GHz is 51 arcsec. We pointed the antenna towards 03:47:32.10 RA (J2000) and 32:56:43.0 Dec. (J2000). Pointing and focus accuracy was checked with observations of SiO masers at 86.2 GHz, and was found to be within 5 arcsec for the pointing. The receiver backend was a FFT spectrometer, consisting of four modules. To increase the effective observation time, we used the dual-polarization mode, covering about 2.5 GHz per module pair. This resulted in 4 GHz total bandwidth per frequency setting, with an overlap of about 1 GHz. The frequency resolution was 76.3 kHz, corresponding to a velocity resolution of 0.31 km s^{-1} at 74 GHz. The data was calibrated using the chopper-wheel method and the estimated calibration uncertainty was 10 per cent. In the 2017, 2018, and 2022 observations, the system noise temperature varied mostly within 195–450, 165–405, and 170–360 K, respectively, but for shorter periods of worse observing conditions it increased significantly above this.

We used the 20 m data reduction software XS for data reduction and correction for frequency- and elevation-dependent main beam efficiency and Doppler-shifted spectral resolution. Spectra with noise temperatures above 500 K were excluded. We combined our 2017 and 2018 data with our 2022-S1 and 2022-S2 data, respectively, and averaged the dual-polarization spectra weighted by their system temperature and integration time. We fitted and subtracted a linear baseline to line-free regions in the 2017-2022-S1 and 2018-2022-S2 averaged spectra, and combined them to one spectrum.

Table 1. Targeted Gly-I and Gly-II transitions and their spectroscopic properties, taken from CDMS (cdms.astro.uni-koeln.de; see also Ilyushin et al. 2005).

Transition	Frequency (GHz)	$E_{\rm u}$ (K)	$A_{\rm ul}$ ($\mathrm{s^{-1}}$)	$g_{\rm u}$ –
Gly-I				
$10_{3,7} - 9_{3,6}$	71.611 56	21.5	1.5×10^{-6}	63
$11_{2,10} - 10_{2\,9}$	71.646 39	22.4	1.6×10^{-6}	69
$10_{2,8} - 9_{2,7}$	71.910 30	20.2	1.6×10^{-6}	63
$12_{1,12} - 11_{1,11}$	72.559 35	23.3	1.8×10^{-6}	75
$12_{0,12} - 11_{0,11}$	72.601 11	23.3	1.8×10^{-6}	75
$11_{1,10} - 10_{1,9}$	72.841 25	22.3	1.7×10^{-6}	69
$6_{3,4} - 5_{2,3}$	73.503 46	9.9	3.5×10^{-7}	39
$11_{3,9} - 10_{3,8}$	74.923 44	24.7	1.8×10^{-6}	69
$4_{4,1} - 3_{3,0}$	75.795 27	8.6	7.2×10^{-7}	27
$4_{4,0} - 3_{3,1}$	75.802 14	8.6	7.2×10^{-7}	27
$11_{4,8} - 10_{4,7}$	75.922 23	27.1	1.8×10^{-6}	69
$11_{4,7} - 10_{4,6}$	76.913 70	27.2	1.8×10^{-6}	69
$6_{3,3} - 5_{2,4}$	77.199 06	9.9	3.7×10^{-7}	39
$12_{2,11} - 11_{2,10}$	77.652 29	26.1	2.1×10^{-6}	75
Gly-II				
$10_{3,8} - 9_{3,7}$	71.141 50	21.7	5.2×10^{-5}	63
$10_{6,5} - 9_{6,4}$	71.614 83	30.2	3.8×10^{-5}	63
$10_{6,4} - 9_{6,3}$	71.617 29	30.2	3.8×10^{-5}	63
$10_{5,6} - 9_{5,5}$	71.877 04	26.8	4.5×10^{-5}	63
$10_{5,5} - 9_{5,4}$	71.942 25	26.8	4.5×10^{-5}	63
$10_{4,7} - 9_{4,6}$	72.065 95	24.0	5.0×10^{-5}	63
$10_{4,6} - 9_{4,5}$	72.944 52	24.0	5.2×10^{-5}	63
$11_{2,10} - 10_{2,9}$	74.121 76	23.1	6.2×10^{-5}	69
$10_{2,8} - 9_{2,7}$	74.838 70	21.0	6.4×10^{-5}	63
$12_{1,12} - 11_{1,11}$	74.926 70	24.1	6.7×10^{-5}	75
$12_{0,12} - 11_{0,11}$	74.950 73	24.1	6.7×10^{-5}	75
$11_{1,10} - 10_{1,9}$	75.009 64	23.0	6.5×10^{-5}	69
$10_{3,7} - 9_{3,6}$	75.378 86	22.2	6.3×10^{-5}	63
$11_{3,9} - 10_{3,8}$	77.916 34	25.4	7.0×10^{-5}	69

3 RESULTING SPECTRUM AND LINE IDENTIFICATION

The resulting spectrum of our observations towards the B5 hotspot is shown in Fig. 2. The frequencies of the targeted Gly-I and Gly-II transitions from Table 1 are marked by solid green and blue lines, respectively. The selection of considered glycine transitions is described in more detail in Section 4.1. The RMS noise towards

[2] http://www.herschel.fr/cea/gouldbelt/en/Phocea/Vie_des_labos/Ast/ast_visu.php?id_ast=66

[3] We used $N(H_2) = 1 \times 10^{22}\,\mathrm{cm^{-2}}$ to update the abundances derived for water and COMs in Wirström et al. (2014) and Taquet et al. (2017).

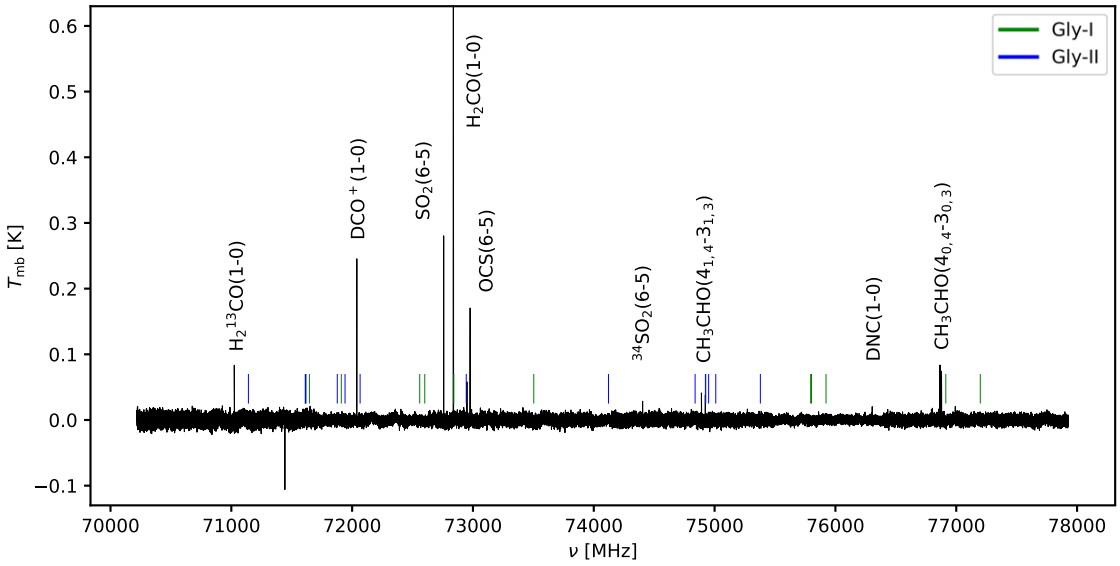

Figure 2. Spectrum towards the B5 methanol hotspot in the frequency range 70.2–77.9 GHz. The solid green and blue lines mark the frequencies of targeted Gly-I and Gly-II transitions, respectively. The peak intensity of the truncated H_2CO(1-0) line is at ∼1.22 K. The negative feature at ∼71.44 GHz and the positive feature at ∼72.95 GHz, left of the OCS(6-5) peak, are bad channels.

the low-frequency end of the spectrum is ∼6.2 mK. It decreases with frequency to reach ∼4.2 mK towards the high-frequency end. In regions where the backend modules overlap, around 72 and 76 GHz, there is a noticeable decrease in noise due to the spectral resampling resulting in an increase of the effective channel width.

None of the targeted glycine lines shows an intensity above the noise level but we use spectral line stacking to derive column density and abundance upper limits for Gly-I and Gly-II, separately. This is described in more detail in Section 4.1.

We do detect emission lines from acetaldehyde (CH_3CHO), formaldehyde (H_2CO; $H_2{}^{13}CO$), the DCO^+ ion, deuterated hydrogen isocyanide (DNC), carbonyl sulfide (OCS), and sulfur dioxide (SO_2; $^{34}SO_2$). The detected transitions are listed in column two of Table 2 together with their line width and integrated intensity (last two columns). The individual spectral lines with their Gaussian fits are shown in Fig. A1.

4 ANALYSIS

4.1 Glycine upper limits

Spectral line stacking is used to derive the highest sensitivity estimates possible for the column density upper limits of Gly-I and Gly-II. Our stacking method consists of four steps:

(1) identification of the presumably strongest transitions,
(2) extraction of spectra around the transition frequencies of the identified transitions,
(3) conversion of intensity scale to column density scale in all spectra, assuming LTE conditions,
(4) averaging of the obtained column density spectra.

Assuming LTE conditions and optically thin emission, the total, beam-averaged column density of a molecule can be written as

$$N_{\rm tot} = \frac{1}{C}\int T_{\rm mb}{\rm d}v, \tag{4}$$

where $\int T_{\rm mb}{\rm d}v$ is the integrated intensity and C is a constant, given as

$$C = \frac{hc^3}{8\pi k_{\rm B}}\frac{g_{\rm u}A_{\rm ul}}{\nu^2}\frac{\exp(-E_{\rm u}/T_{\rm ex})}{Q_{\rm rot}(T_{\rm ex})}\left[1-\frac{J_\nu(T_{\rm bg})}{J_\nu(T_{\rm ex})}\right]. \tag{5}$$

h is the Planck constant, c is the speed of light, $k_{\rm B}$ is the Boltzmann constant, $T_{\rm ex}$ is the excitation temperature, and $T_{\rm bg}$ is the CMB temperature. The line-specific spectroscopic parameters are the total degeneracy $g_{\rm u}$, Einstein coefficient for spontaneous emission $A_{\rm ul}$, transition (rest) frequency ν, upper state energy $E_{\rm u}$ (in Kelvin), and the rotational partition function $Q_{\rm rot}$ at $T = T_{\rm ex}$. Furthermore, $J_\nu(T)$ is the temperature equivalent of the specific intensity, given as

$$J_\nu(T) = \frac{h\nu}{k_{\rm B}}\left[\exp\left(\frac{h\nu}{k_{\rm B}T}\right)-1\right]^{-1}. \tag{6}$$

The last term in equation (5) is only needed if $T_{\rm ex}$ is comparable to $T_{\rm bg}$, which is the case for the B5 hotspot. According to equation (4), the column density in one spectral channel of width Δv is given by

$$N_{\rm tot}^{\rm ch} = \frac{T_{\rm A}^{\rm ch}\Delta v}{C}, \tag{7}$$

and for step (1), we estimate the antenna temperature in one channel ($T_{\rm A}^{\rm ch}$) for all Gly-I and Gly-II transitions in the frequency range 70.2–77.9 GHz. We assume $N_{\rm tot}^{\rm ch} = 3.6\times10^{12}\,{\rm cm}^{-2}$ for Gly-I and $N_{\rm tot}^{\rm ch} = 2.0\times10^{11}\,{\rm cm}^{-2}$ for Gly-II, and set $\Delta v = 0.4\,{\rm km\,s}^{-1}$ and $T_{\rm ex} = 7.5$ K, based on temperature estimates for the B5 methanol hotspot (Taquet et al. 2017). Only transitions for which $T_{\rm A}^{\rm ch} > T_{\rm lim}$ are considered, and we use 2 and 1 mK as temperature limits $T_{\rm lim}$ for Gly-I and Gly-II, respectively. The considered transitions are listed in Table 1, together with the spectroscopic parameters that feed into the constant C, i.e. $E_{\rm u}$, $A_{\rm ul}$, and $g_{\rm u}$. The rotational partition functions of Gly-I and Gly-II are 1350.38 and 1310.26 at $T = 9.375$ K, respectively (values from CDMS[4]; see also Ilyushin et al. 2005). Based on the theoretical temperature dependence for the rotational

[4]cdms.astro.uni-koeln.de

Table 2. Detected transitions with their spectroscopic and observed parameters; all uncertainties are 1σ values. Spectroscopic parameters are taken from CDMS (cdms.astro.uni-koeln.de) and JPL (spec.jpl.nasa.gov; only for CH_3CHO; see also Kleiner, Lovas & Godefroid 1996).

Molecule	Transition	ν (GHz)	E_u (K)	A_{ul} (s^{-1})	g_u	$Q_{rot}(9.375\,K)$	FWHM$^{(a)}$ ($km\,s^{-1}$)	$\int T_{mb}dv$ $^{(b)}$ ($mKkm\,s^{-1}$)
A − CH_3CHO	$4_{14} - 3_{13}$	74.891 67	11.3	1.3×10^{-5}	9$^{(c)}$	66.02$^{(d)}$	0.67 ± 0.07	30.2 ± 3.3
	$4_{04} - 3_{03}$	76.878 95	9.2	1.5×10^{-5}	9$^{(c)}$	66.02$^{(d)}$	0.51 ± 0.06	45.8 ± 2.8
E − CH_3CHO	$4_{14} - 3_{13}$	74.924 13	11.3	1.3×10^{-5}	9$^{(c)}$	66.02$^{(d)}$	0.75 ± 0.10	27.0 ± 2.7
	$4_{04} - 3_{03}$	76.866 43	9.3	1.5×10^{-5}	9$^{(c)}$	66.02$^{(d)}$	0.67 ± 0.03	60.8 ± 2.9
H_2CO	$1_{01} - 0_{00}$	72.837 94	3.5	8.2×10^{-6}	3	13.80	1.04 ± 0.04	1370.1 ± 3.8
$H_2{}^{13}CO$	$1_{01} - 0_{00}$	71.024 78	3.4	7.6×10^{-6}	3	14.13	0.77 ± 0.07	69.3 ± 4.9
DCO^+	$1 - 0$	72.039 31	3.5	2.3×10^{-5}	3	5.77	1.29 ± 0.06	331.6 ± 3.0
DNC	$1 - 0$	76.305 73	3.7	1.6×10^{-5}	3	5.47	1.92 ± 0.27	29.1 ± 2.4
OCS	$6 - 5$	72.976 77	12.3	1.1×10^{-6}	13	32.46	0.60 ± 0.03	102.2 ± 3.5
SO_2	$6_{06} - 5_{15}$	72.758 24	19.2	2.8×10^{-6}	13	33.07	0.70 ± 0.02	220.5 ± 4.0
$^{34}SO_2$	$6_{06} - 5_{15}$	74.404 57	19.1	3.0×10^{-6}	13	33.64	0.49 ± 0.13	14.0 ± 2.6

Notes. (*a*) Derived from Gaussian fits (see Fig. A1); (*b*) Derived by integration over line channels (see Fig. A1).
(*c*) We use $g_u = 2J + 1$ to be consistent with $Q_{rot}(T)$ from Nummelin et al. (1998).
(*d*) From Nummelin et al. (1998) for A-/E-species separated, i.e. $Q_{rot}(T) = 2.3 \times T^{3/2}$.

partition function of (a)symmetric-top molecules, we determine the partition function at T_{ex} as

$$Q_{rot}(T_{ex}) = Q_{rot}(T)\left(\frac{T_{ex}}{T}\right)^{3/2}. \quad (8)$$

As step (2), we extract spectra over 50 $km\,s^{-1}$ around the transition frequencies of the considered Gly-I and Gly-II transitions, and determine 1σ noise temperatures T_{mb}^{σ} in line-free regions (compare Figs A2 and A3). In order to obtain a single column density estimate from the obtained spectra, the individual spectroscopic line parameters must be included before averaging. In step (3), we do this by transferring the intensity axis of each spectrum to a column density axis by using

$$N_{tot}(v) = \frac{T_{mb}(v)\Delta v}{C}, \quad (9)$$

where $T_{mb}(v)$ is the observed main beam temperature. Finally, as step (4), we average the obtained column density spectra weighted by 1σ noise column density, which we calculate for all spectra as

$$N_{tot}^{\sigma} = \frac{T_{mb}^{\sigma}\Delta v}{C}. \quad (10)$$

The stacked column density spectra for Gly-I and Gly-II are shown in Fig. 3. Even in the stacked spectra, glycine is still not detected, but we use the obtained noise level to derive sensitive upper limits. In both spectra, the dashed blue line marks the 1σ column density noise level. The corresponding 3σ column density upper limits of Gly-I and Gly-II are presented in Table 3 together with the abundance upper limits relative to H_2.

4.2 Column densities of detected species

Column densities of H_2CO, $H_2{}^{13}CO$, DCO^+, DNC, OCS, SO_2, and $^{34}SO_2$ are calculated from equation (4), assuming LTE conditions and optically thin emission. The required spectroscopic parameters are given in Table 2, and we use equation (8) to determine the rotational partition functions at $T_{ex} = 7.5$ K. For the linear molecules DNC and OCS, we use the equivalent relation

$$Q_{rot}(T_{ex}) = Q_{rot}(T)\frac{T_{ex}}{T}. \quad (11)$$

In the case of the H_2CO(1-0) line, we expect the optically thin approximation to fail, and derive an estimate for the optical depth τ using the rare isotopologue method with

$$\frac{W_{12}}{W_{13}} = [1 - \exp(-\tau)]\left[1 - \exp\left(\frac{-\tau}{^{12}C/^{13}C}\right)\right]^{-1}, \quad (12)$$

where W_{12} and W_{13} are the integrated intensities of H_2CO(1-0) and $H_2{}^{13}CO$(1-0), respectively. We assume $^{12}C/^{13}C = 68$ for the local ISM, based on Milam et al. (2005). We get $\tau = 3.4$ and calculate the corrected column density of H_2CO using

$$N_{tot}^{corr} = \frac{\tau}{1 - \exp(-\tau)}N_{tot}^{thin}, \quad (13)$$

where N_{tot}^{thin} is the optically thin estimate.

The derived column densities are presented in Table 3, together with the molecular abundances relative to H_2.

4.3 Rotation diagram acetaldehyde

Following Goldsmith & Langer (1999), we perform a rotation diagram analysis for the four detected transitions of acetaldehyde (CH_3CHO), listed in Table 2, together with six transitions detected towards the B5 hotspot by Taquet et al. (2017). We assume optically thin emission and an LTE population of levels, and calculate the upper state column densities N_u as

$$N_u = \frac{8\pi k_B \nu^2}{A_{ul}hc^3}\int T_{mb}dv. \quad (14)$$

Plotting $\ln(N_u/g_u)$ against E_u and fitting the data linearly yields an excitation temperature of $T_{ex} = 5.8 \pm 0.8$ K and a total column density of $N_{tot} = (1.4 \pm 0.5) \times 10^{12}\,cm^{-2}$. Fitting the data for A- and E-species separately yields approximately the same result as fitting the data for both species combined, as expected from the low difference in ground state energy (0.1 K; Kleiner et al. 1996). When finding an excitation temperature so close to the CMB temperature ($T_{bg} = 2.73$ K) it is important to consider its influence on excitation using the correction term

$$C_{bg} = \left[1 - \frac{J_\nu(T_{bg})}{J_\nu(T_{ex})}\right]^{-1}. \quad (15)$$

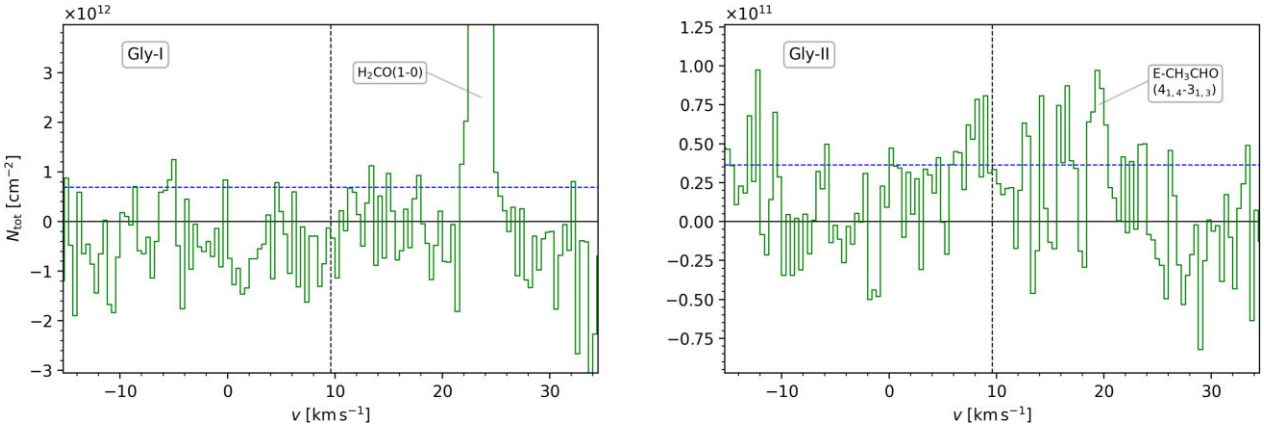

Figure 3. Stacked spectra for Gly-I (left) and Gly-II (right) in column density scale, determined from equation (9). In both spectra, the dashed blue line marks the 1σ column density noise level, and the dashed black line marks the LSR velocity of the B5 methanol hotspot. The column density peaks at $\sim 24\,\mathrm{km\,s^{-1}}$ (left) and $\sim 20\,\mathrm{km\,s^{-1}}$ (right) arise from the detected $H_2CO(1\text{-}0)$ and $CH_3CHO(4_{1,4}\text{-}3_{1,3})$ transitions, respectively. The regions where the peaks appear are excluded from the RMS calculation (compare Figs A2 and A3).

Table 3. Beam-averaged column densities and abundances relative to H_2; uncertainties are 1σ values and upper limits are 3σ values. We use $N(H_2) = 1 \times 10^{22}\,\mathrm{cm^{-2}}$ from HGBS data (Roy et al. 2014).

Molecule	N_{tot} ($\mathrm{cm^{-2}}$)	$N_{tot}/N(H_2)$
$CH_3CHO^{(a)}$	$(1.97 \pm 0.65) \times 10^{12}$	2×10^{-10}
H_2CO	$(4.14 \pm 0.01) \times 10^{13}$	4×10^{-9}
$H_2{}^{13}CO$	$(6.20 \pm 0.44) \times 10^{11}$	6×10^{-11}
DCO^+	$(4.14 \pm 0.04) \times 10^{11}$	4×10^{-11}
DNC	$(6.27 \pm 0.51) \times 10^{10}$	6×10^{-12}
OCS	$(1.31 \pm 0.04) \times 10^{13}$	1×10^{-9}
SO_2	$(2.48 \pm 0.04) \times 10^{13}$	3×10^{-9}
$^{34}SO_2$	$(1.54 \pm 0.28) \times 10^{12}$	2×10^{-10}
Gly-I	$\leq 4.6 \times 10^{12}$ (b)	$\leq 5 \times 10^{-10}$ (b)
	$\leq 2.1 \times 10^{12}$ (c)	$\leq 2 \times 10^{-10}$ (c)
	$\leq 1.6 \times 10^{12}$ (d)	$\leq 2 \times 10^{-10}$ (d)
Gly-II	$\leq 3.3 \times 10^{11}$ (b)	$\leq 3 \times 10^{-11}$ (b)
	$\leq 1.1 \times 10^{11}$ (c)	$\leq 1 \times 10^{-11}$ (c)
	$\leq 7.1 \times 10^{10}$ (d)	$\leq 7 \times 10^{-12}$ (d)

Notes. (*a*) $T_{ex} = 5.7\,\mathrm{K}$, from CH_3CHO rotation diagram analysis. (*b*) $T_{ex} = 5\,\mathrm{K}$; (*c*) $T_{ex} = 7.5\,\mathrm{K}$; (*d*) $T_{ex} = 10\,\mathrm{K}$.

The corrected upper state column density is then given by

$$N_u^{corr} = C_{bg}\, N_u. \quad (16)$$

Iterating the updated values of N_u^{corr} and T_{ex}, the asymptotic values of excitation temperature and total column density are $T_{ex} = 5.7\,\mathrm{K}$ and $N_{tot} = (2.0 \pm 0.6) \times 10^{12}\,\mathrm{cm^{-2}}$. The resulting abundance relative to H_2 is 2×10^{-10} (see Table 3). The final rotation diagram is shown in Fig. 4. For the calculation of total column density, we use the rotational partition function derived in Nummelin et al. (1998) as $Q_{rot}(T) = 4.6 \times T^{3/2}$ for A- and E-species combined, and for $g_u = 2J + 1$. Considering both species separately using the same iterative process as described gives an A/E ratio of 0.88, which is close to the expected ratio of unity.

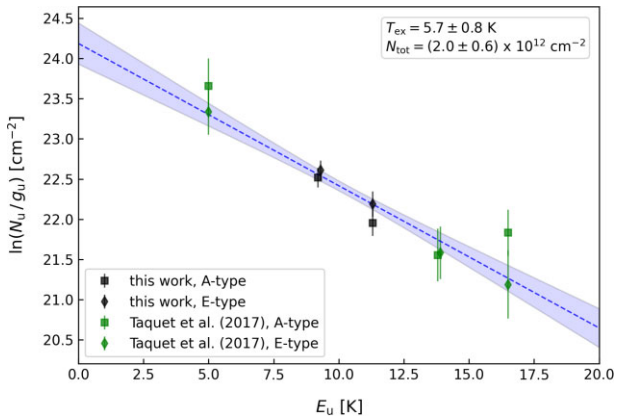

Figure 4. Rotation diagram for acetaldehyde (CH_3CHO) transitions detected in this work (black symbols) and in Taquet et al. (2017; green symbols) towards the B5 methanol hotspot. A- and E-type transitions are depicted as squares and diamonds, respectively. The best linear fit to the data is shown as dashed blue line with 1σ confidence interval (shaded blue area). Considering the influence of cosmic microwave background (CMB) radiation, the resulting excitation temperature is $5.7 \pm 0.8\,\mathrm{K}$, and the total column density is $(2.0 \pm 0.6) \times 10^{12}\,\mathrm{cm^{-2}}$.

5 DISCUSSION

The excitation temperature of $5.7 \pm 0.8\,\mathrm{K}$ obtained from the CH_3CHO data indicates possible sub-thermal excitation of the rotational levels of acetaldehyde at the position of the B5 hotspot (where the gas kinetic temperature is estimated from methanol lines as $T_{kin} = 7.5 \pm 1.5\,\mathrm{K}$). Based on that, and in order to cover a larger range of possible excitation temperatures for glycine, we calculate two more sets of 3σ upper limits for 5 and 10 K (see Table 3). For the lower excitation limit of $T_{ex} = 5\,\mathrm{K}$, the number of considered Gly-I and Gly-II transitions in the spectral line stacking reduces to two and 10, respectively, and the abundance upper limits increase to 5×10^{-10} and 3×10^{-11}. Conversely, for the higher excitation limit of $T_{ex} = 10\,\mathrm{K}$, the number of considered Gly-I and Gly-II transitions increases to 18 and 16, respectively. The abundance upper limit of Gly-I remains at rounded 2×10^{-10}, while that of Gly-II decreases to 7×10^{-12}.

5.1 Glycine upper limits compared to other sources

Few previous attempts have been made to detect glycine towards cold low mass sources. The published upper limits we have identified

Table 4. Glycine upper limits (3σ) towards cold molecular cloud sources.

Source	Conformer	T_{ex} (K)	N_{upper} (cm^{-2})	$N_{upper}/N(H_2)$	Reference
L1544 Dust peak	Gly-I	5	5.8×10^{12}	1×10^{-10}	(1)
		10	3.3×10^{12}	6×10^{-11}	
L1544 Methanol peak	Gly-I	5	9.5×10^{12}	6×10^{-10}	(1)
		10	4.2×10^{12}	3×10^{-10}	
IRAS16293-2422	Gly-I	20	5.0×10^{12}	1×10^{-10}	(2)
L134	Gly-II	10	2.0×10^{12}	2×10^{-10}	(3), (4)[(a)]
TMC-1	Gly-II	7	3.0×10^{12}	2×10^{-10}	(5), (6)[(a)]
L183	Gly-II	7	4.5×10^{12}	2×10^{-10}	(5), (7)[(a)]

Notes (1) Jiménez-Serra et al. (2016); (2) Ceccarelli et al. (2000); (3) Snyder et al. (1983); (4) van der Werf et al. (1988); (5) Brown et al. (1979); (6) Spezzano et al. (2022); (7) Lattanzi et al. (2020)
(*a*) Reference for source H_2 column density.

are summarized in Table 4. 3σ upper limits[5] of Gly-II are reported for the dark clouds TMC-1 and L183 in Brown et al. (1979) as 3×10^{12} cm^{-2} and 4.5×10^{12} cm^{-2}, respectively, assuming $T_{ex} =$ 7 K for both sources. Another 3σ upper limit of Gly-II is reported in Snyder et al. (1983) for L134 as 2×10^{12} cm^{-2}, assuming $T_{ex} = 10$ K. Adopting the respective H_2 column densities towards TMC-1, L183, and L134 (2×10^{22}, 3×10^{22}, and 1×10^{22} cm^{-2}; van der Werf, Goss & Vanden Bout 1988; Lattanzi et al. 2020; Spezzano et al. 2022), the corresponding Gly-II abundance upper limits are presented in Table 4. Depending on the assumed excitation temperature at the B5 hotspot, the Gly-II abundance upper limit of this work is one to two orders of magnitude lower than those early estimates.

Jiménez-Serra et al. (2016) report two sets of 3σ upper limits for Gly-I towards the centre of the pre-stellar core L1544 and an offset position towards the shell-region where methanol emission is found to peak (see Table 4). The assumed excitation temperatures are 5 and 10 K. Based on typical COM excitation temperatures of ∼5–6 K, reported for the L1544 dust peak, the upper limit estimate for $T_{ex} = 5$ K might be better constrained at that position. It is on the same order than our Gly-I upper limit towards the B5 hotspot. At $T_{ex} = 10$ K, the upper limit at the L1544 dust peak becomes an order of magnitude lower than the limit at the B5 hotspot. Typical COM excitation temperatures at the L1544 methanol peak are reported as ∼5–8 K. At both excitation limits ($T_{ex} = 5$ and 10 K), the Gly-I abundance upper limit towards the B5 hotspot is slightly lower but on the same order as at the L1544 methanol peak. We note that the conditions at the L1544 methanol peak are presumably more similar to the B5 methanol hotspot than the conditions at the L1544 dust peak.

Another 3σ upper limit of Gly-I is reported for the cold (∼20 K) outer layer of the solar-type protostar IRAS16293-2422 in Ceccarelli et al. (2000) as 5×10^{12} cm^{-2}, i.e. 1×10^{-10} w.r.t. $N(H_2)$. The upper limit is obtained by averaging over three lines at around 101 GHz. However, the assumed excitation conditions in the envelope of IRAS16293-2422, though cold, are only marginally comparable to the case of the B5 hotspot because a difference of ≥10 K in excitation temperature is quite significant at low temperatures, and can change an upper limit by about an order of magnitude.

5.2 Glycine upper limits compared to COM abundances at the B5 hotspot

The acetaldehyde column density we derive in our study, i.e. $(2.0 \pm 0.6) \times 10^{12}$ cm^{-2}, is approximately 2.5 times lower than the estimate in Taquet et al. (2017), i.e. $(5.2 \pm 0.7) \times 10^{12}$ cm^{-2}. This discrepancy cannot be explained by the higher number of available data points for the rotation diagram analysis, but we are confident about the updated estimate.

The abundances of COMs relative to H_2 at the hotspot range from 2×10^{-10} for acetaldehyde and 4×10^{-10} for methyl formate to 2×10^{-8} for methanol; di-methyl ether is tentatively detected at 2×10^{-10} (Taquet et al. 2017). The most stringent, total abundance upper limit of glycine derived from the present observations (2×10^{-10} for $T_{ex} = 7.5$ K) is comparable to the abundance of the least abundant COM so far detected at the hotspot. Hence, given the present data, we can neither confirm nor rule out the presence of glycine in the gas phase at the B5 hotspot. If glycine is present but undetected, it is either less abundant than other COMs or has a more compact distribution or both.

6 CONCLUSIONS

Using the Onsala 20 m telescope, we performed a deep search for glycine towards the B5 methanol hotspot, which is a cold source ($T_k \approx 7.5$ K) with yet a significant amount of COMs in the gas phase (Taquet et al. 2017). We targeted several transitions of Gly-I and Gly-II in the frequency range ∼70–78 GHz. Our study is the first to search for a set of glycine transitions in this lower frequency range.

We did neither detect Gly-I nor Gly-II during our observations but derive sensitive upper limits for both conformers, using spectral line stacking and assuming LTE conditions and optically thin emission. Since, we did not detect glycine the hypothesis of a non-equilibrium Gly-II/Gly-I ratio similar to the case of *c*-HCOOH/*t*-HCOOH could not be tested. Our Gly-II upper limits towards the B5 hotspot are the most stringent obtained so far for a cold molecular cloud source. The obtained Gly-I limits are mostly on the same order as previously published limits towards comparable sources.

If glycine is present but undetected in the gas phase at the B5 hotspot it is either less abundant than other detected COMs in that source or has a more compact distribution or a combination thereof. We, therefore, do not rule out a future detection of glycine towards the B5 hotspot with higher-sensitivity instrumentation. Jiménez-Serra et al. (2014) calculate a detection limit of $\sim 1.5 \times 10^{-11}$ for glycine in cold molecular cloud sources. This limit has not yet been reached by any study searching for glycine.

ACKNOWLEDGEMENTS

The authors acknowledge support from Onsala Space Observatory for the provisioning of its facilities/observational support. The Onsala

[5]Reported are 2σ limits from which we derived 3σ values.

Space Observatory national research infrastructure is funded through Swedish Research Council grant No 2017-00648. This work was supported by Chalmers' Gender Initiative for Excellence (Genie) and the Goddard Center for Astrobiology. This research has made use of data from the Herschel Gould Belt Survey (HGBS) project (http://gouldbelt-herschel.cea.fr). The HGBS is a Herschel Key Programme jointly carried out by SPIRE Specialist Astronomy Group 3 (SAG 3), scientists of several institutes in the PACS Consortium (CEA Saclay, INAF-IFSI Rome and INAF-Arcetri, KU Leuven, MPIA Heidelberg), and scientists of the Herschel Science Center (HSC). We are grateful to Jose Aponte for preparing Fig. 1, to Henrik Olofsson for assistance with the observations and discussions regarding the data reduction, and to the anonymous reviewer whose comments helped to improve the content of the paper.

DATA AVAILABILITY

The data underlying this article will be shared on reasonable request to the corresponding author.

REFERENCES

Agúndez M., Marcelino N., Cernicharo J., Roueff E., Tafalla M., 2019, A&A, 625, A147
Altwegg K. et al., 2016, Sci. Adv., 2, e1600285
André P. et al., 2010, A&A, 518, L102
Bacmann A., Taquet V., Faure A., Kahane C., Ceccarelli C., 2012, A&A, 541, L12
Belitsky V. et al., 2015, A&A, 580, A29
Belloche A., Menten K., Comito C., Müller H. S. P., Schilke P., Ott J., Thorwirth S., Hieret C., 2008, A&A, 482, 179
Bernstein M., Dworkin J., Sandford S., Cooper G., Allamandola L., 2002, Nature, 416, 401
Berulis I., Winnewisser G., Krasnov V., Sorochenko R., 1985, Sov. Astron. Lett., 11, 251
Botta O., Glavin D., Kminek G., Bada J., 2002, Orig. Life Evol. Biosph., 32, 143
Brown R. et al., 1979, MNRAS, 186, 5P
Brown R., Godfrey P., Storey J., Bassez M., 1978, J. Chem. Soc. Chem. Commun., 13, 547
Ceccarelli C., Loinard L., Castets A., Faure A., Lefloch B., 2000, A&A, 355, 1129
Combes F., Rieu N.-Q., Wlodarczak G., 1996, A&A, 308, 618
Cronin J., Pizzarello S., 1999, Adv. Space Res., 23, 91
Cuadrado S., Goicoechea J. R., Roncero O., Aguado A., Tercero B., Cernicharo J., 2016, A&A, 596, L1
Cunningham M. et al., 2007, MNRAS, 376, 1201
Drozdovskaya M. N., van Dishoeck E. F., Rubin M., Jørgensen J. K., Altwegg K., 2019, MNRAS, 490, 50
Ehrenfreund P., Charnley S., 2000, ARA&A, 38, 483
Ehrenfreund P., Glavin D., Botta O., Cooper G., Bada J., 2001, Proc. Natl. Acad. Sci., 98, 2138
Elsila J., Glavin D., Dworkin J., 2009, Meteorit. Planet. Sci., 44, 1323
Enrique-Romero J., Rimola A., Ceccarelli C., Balucani N., 2016, MNRAS, 459, L6
Friberg P., Madden S., Hjalmarson A., Irvine W., 1988, A&A, 195, 281
García de la Concepción J. et al., 2022, A&A, 658, A150
Garrod R. T., Jin M., Matis K. A., Jones D., Willis E. R., Herbst E., 2022, ApJS, 259, 1
Garrod R., 2013, ApJ, 765, 29
Glavin D., Dworkin J., Aubrey A., Botta O., Doty J. H., Martins Z., Bada J. L., 2006, Meteorit. Planet. Sci., 41, 889
Goldsmith P. F., Langer W. D., 1999, ApJ, 517, 209
Goumans T., Uppal M., Brown W., 2008, MNRAS, 384, 1158
Guélin M., Brouillet N., Cernicharo J., Combes F., Wooten A., 2008, Astrophys. Space Sci., 313, 45
Guélin M., Cernicharo J., 1989, in Winnewisser G., Armstrong J., eds, Lecture Notes in Physics, Vol. 331, The Physics and Chemistry of Interstellar Molecular Clouds . Springer-Verlag, Berlin
Hadraoui K. et al., 2019, A&A, 630, 1
Hollis J., Pedelty J., Snyder L., Jewell P. R., Lovas F. J., Palmer P., Liu S.-Y., 2003a, ApJ, 588, 353
Hollis J., Pedelty J., Boboltz D., Liu S.-Y., Snyder L. E., Palmer P., Lovas F. J., Jewell P. R., 2003b, ApJ, 596, L235
Hollis J., Snyder L., Suenram R., Lovas F., 1980, ApJ, 241, 1001
Holtom P., Bennett C., Osamura Y., Mason N., Kaiser R., 2005, ApJ, 626, 940
Hoyle F., Wickramasinghe N., 1977, Nature, 270, 701
Ilyushin V., Alekseev E., Dyubko S., Motiyenko R., Lovas F., 2005, J. Mol. Spectrosc., 231, 15
Ioppolo S. et al., 2021, Nat. Astron., 5, 197
Jiménez-Serra I. et al., 2020, Astrobiology, 20, 1048
Jiménez-Serra I. et al., 2016, ApJL, 830, L6
Jiménez-Serra I., Testi L., Caselli P., Viti S., 2014, ApJL, 787, L33
Jones P., Cunningham M., Godfrey P., Cragg D., 2007, MNRAS, 374, 579
Kleiner I., Lovas F. J., Godefroid M., 1996, J. Phys. Chem. Ref. Data, 25, 1113
Koga T., Naraoka H., 2017, Sci. Rep., 7, 636
Kuan Y.-J., Charnley S., Huang H.-C., Tseng W.-L., Kisiel Z., 2003, ApJ, 593, 848
Kvenvolden K., Lawless J., Pering K., Peterson E., Flores J., Ponnamperuma C., Kaplan I. R., Moore C., 1970, Nature, 228, 923
Lattanzi V., Bizzocchi L., Vasyunin A. I., Harju J., Giuliano B. M., Vastel C., Caselli P., 2020, A&A, 633, A118
Lee C.-W., Kim J.-K., Moon E.-S., Minh Y., Kang H., 2009, ApJ, 697
Lovas F. J., Kawashima Y., Grabow J. U., Suenram R. D., Fraser G. T., Hirota E., 1995, ApJ, 455, L201
Marcelino N., Cernicharo J., Agúndez M., Roueff E., Gerin M., Martin-Pintado J., Mauersberger R., Thum C., 2007, ApJ, 665, L127
Matthews H., Friberg P., Irvine W., 1985, ApJ, 290, 609
Milam S. N., Savage C., Brewster M. A., Ziurys L. M., Wyckoff S., 2005, ApJ, 634, 1126
Müller H. S. P., Schlöder F., Stutzki J., Winnewisser G., 2005, J. Mol. Struct., 742, 215
Müller H. S. P., Thorwirth S., Roth D. A., Winnewisser G., 2001, A&A, 370, L49
Muñoz Caro G. et al., 2002, Nature, 416, 403
Naraoka H. et al., 2023, Science, 379, abn9033
Nummelin A., Dickens J. E., Bergman P., Hjalmarson A., Irvine W. M., Ikeda M., Ohishi M., 1998, A&A, 337, 275
Pickett H. M., Poynter R. L., Cohen E. A., Delitsky M. L., Pearson J. C., Müller H. S. P., 1998, JQSRT, 60, 883
Rimola A., Sodupe M., Ugliengo P., 2012, ApJ, 754, 24
Roy A. et al., 2014, A&A, 562, A138
Snyder L. et al., 2005, ApJ, 619, 914
Snyder L., Hollis J., Suenram R., Lovas F. J., Brown L. W., Buhl D., 1983, ApJ, 268, 123
Sorrell W., 2001, ApJ, 555, L129
Spezzano S. et al., 2022, A&A, 657, A10
Suenram R., Lovas F., 1978, J. Mol. Spectrosc., 72, 372
Suenram R., Lovas F., 1980, J. Am. Chem. Soc., 102, 9
Taquet V., Wirström E., Charnley S., Faure A., López-Sepulcre A., Persson C. M., 2017, A&A, 607, 14
van der Werf P. P., Goss W. M., Vanden Bout P. A., 1988, A&A, 201, 311
Vastel C., Ceccarelli C., Lefloch B., Bachiller R., 2014, ApJL, 795, 6
Walker G. W., Kalinauskaite E., McCarthy D. N., Trappe N. A., Murphy A., Helldner L., Pantaleev M. G., Flygare J., 2016, in Holland W. S., Zmuidzinas J., eds, SPIE Conf. Ser. Vol. 9914, Millimeter, Submillimeter, and Far-Infrared Detectors and Instrumentation for Astronomy VIII. SPI, Bellingham, p. 99142V
Wirström E., Charnley S. B., Persson C. M., Buckle J. V., Cordiner M. A., Takakuwa S., 2014, ApJL, 788, 6
Woon D., 2002, ApJ, 571, L177
Zucker C., Schlafly E. F., Speagle J. S., Green G. M., Portillo S. K. N., Finkbeiner D. P., Goodman A. A., 2018, ApJ, 869, 83

APPENDIX A: ADDITIONAL FIGURES

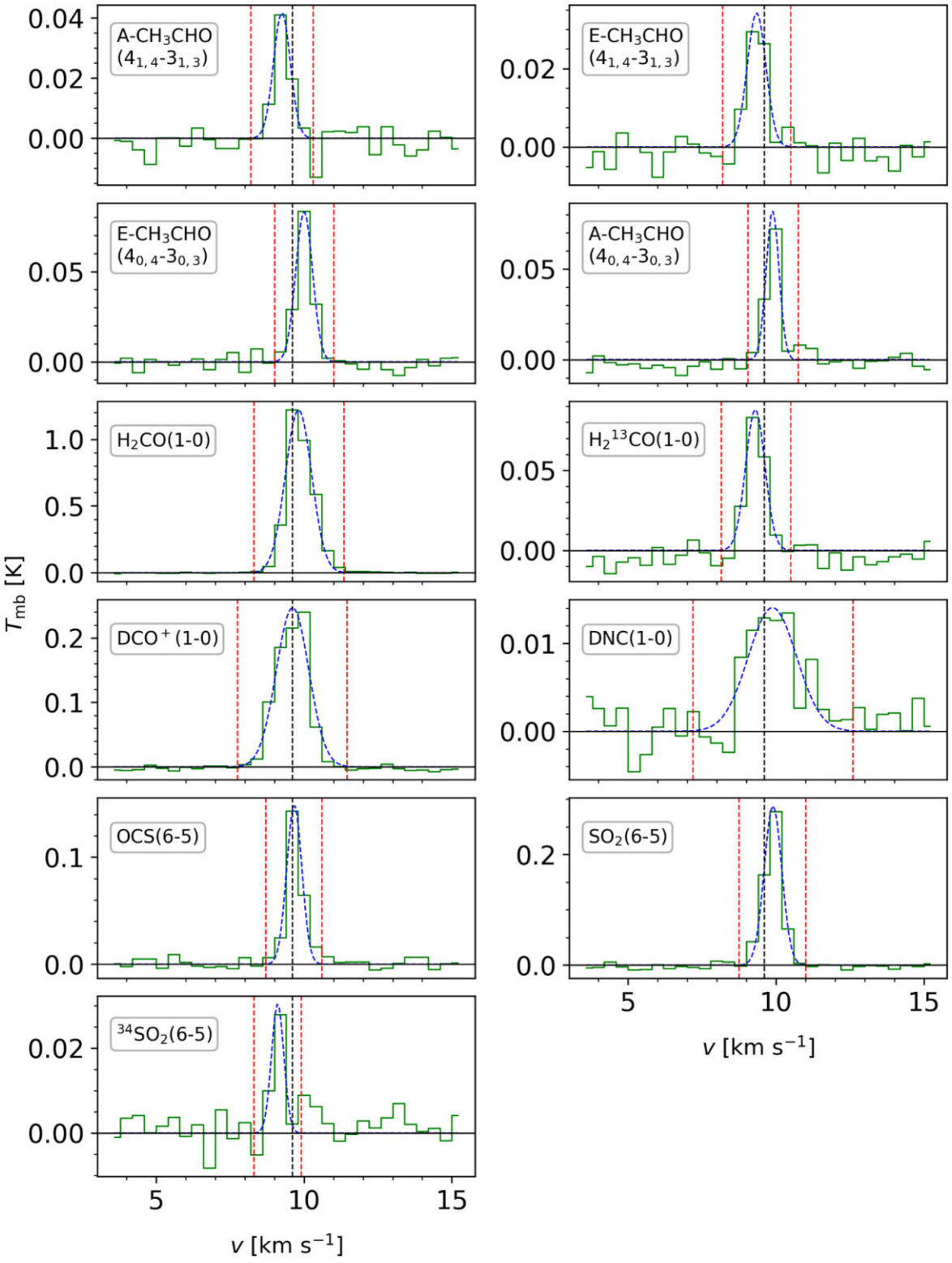

Figure A1. Spectral lines of non-targeted molecular transitions observed in the frequency range 70.2–77.9 GHz towards the B5 methanol hotspot. In all panels, the dashed blue line shows the Gaussian fit of the spectral line, and the dashed black line marks the LSR velocity of the hotspot. The dashed red lines mark the boundaries for the integrated intensity calculation.

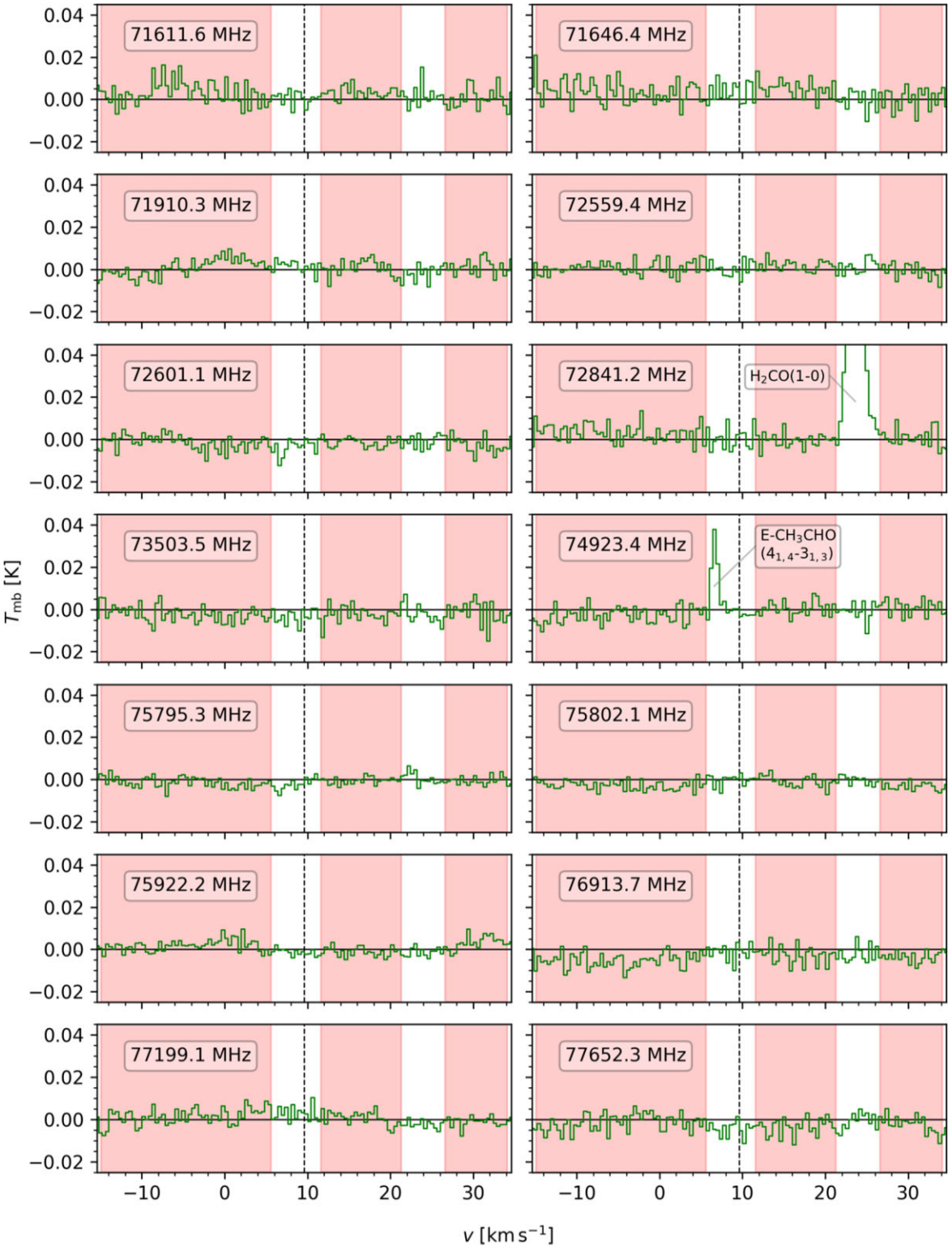

Figure A2. Spectra around transition frequencies of targeted Gly-I transitions. The red regions mark the ranges for the calculation of the RMS noise temperature. The dashed black line marks the LSR velocity of the B5 methanol hotspot.

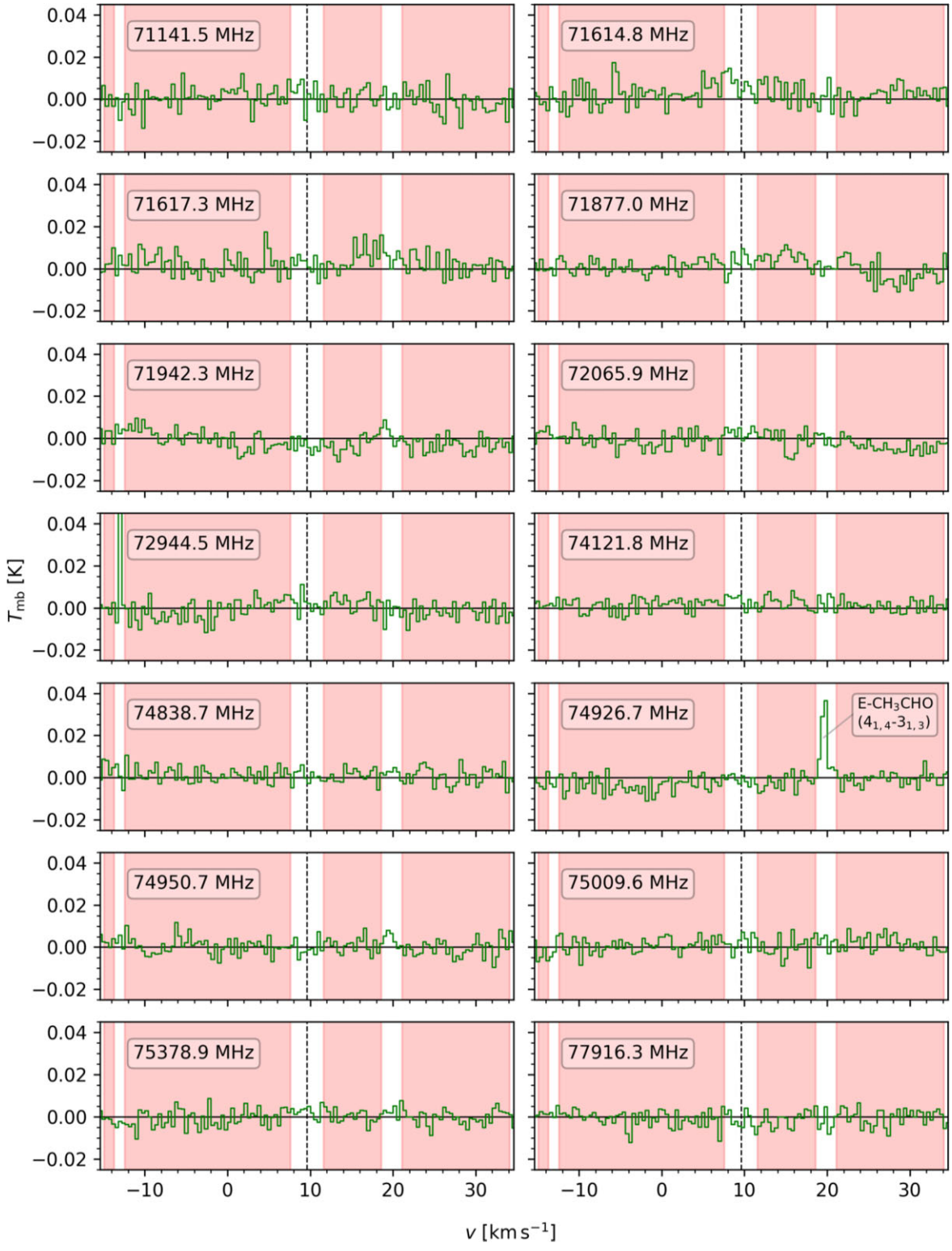

Figure A3. Spectra around transition frequencies of targeted Gly-II transitions. The red regions mark the ranges for the calculation of the RMS noise temperature. The dashed black line marks the LSR velocity of the B5 methanol hotspot.

This paper has been typeset from a TEX/LATEX file prepared by the author.